catalysts

MDPI

Article

Efficient and Stable Degradation of Triazophos Pesticide by TiO_2/WO_3 Nanocomposites with S-Scheme Heterojunctions and Oxygen Defects

Wen Li [1], Chunxu Chen [1], Renqiang Yang [1], Shuangli Cheng [1], Xiaoyu Sang [1], Meiwen Zhang [1], Jinfeng Zhang [2,*], Zhenghua Wang [3] and Zhen Li [1,*]

[1] College of Food Engineering, Anhui Science and Technology University, Chuzhou 233100, China; yjs2022273@ahstu.edu.cn (W.L.); ccx1205@126.com (C.C.); 18954105864@163.com (R.Y.); 15249929336@163.com (S.C.); sanghuaiyu@163.com (X.S.); 13866908959@163.com (M.Z.)

[2] Anhui Province Key Laboratory of Pollutant Sensitive Materials and Environmental Remediation, School of Physics and Electronic Information, Huaibei Normal University, Huaibei 235000, China

[3] Key Laboratory of Functional Molecular Solids, Ministry of Education, College of Chemistry and Materials Science, Anhui Normal University, Wuhu 241000, China; zhwang@ahnu.edu.cn

* Correspondence: jfzhang@chnu.edu.cn (J.Z.); lizhen@ahstu.edu.cn (Z.L.)

Abstract: The prevalent utilization of organophosphorus pesticides presents a profound risk to the global environment, necessitating the immediate development of a secure and reliable methodology to mitigate this hazard. Photocatalytic technology, through the generation of robust oxidizing free radicals by suitable catalysts, offers a viable solution by effectively oxidizing organophosphorus pesticides, thus preserving environmental well-being. In this study, we successfully synthesized TiO_2/WO_3 (TO/WO) nanocomposites characterized by oxygen defects and S-scheme heterojunctions, demonstrating superior photocatalytic activity in the degradation of triazophos. Notably, the 60-TO/WO nanocomposite, wherein the proportion of WO comprises 60% of the total, exhibited optimal photocatalytic degradation activity, achieving a degradation rate of 78% within 120 min, and demonstrating exceptional stability, maintaining impressive degradation activity across four cycles. This performance was notably superior to that of standalone TO and WO. The presence of oxygen defects in WO was corroborated by electron paramagnetic resonance (EPR) spectroscopy. The mechanism at the heterojunction of the 60-TO/WO nanocomposite, identified as an S-scheme, was also confirmed by EPR and theoretical computations. Oxygen defects expedite charge transfer and effectively enhance the photocatalytic reaction, while the S-scheme effectively segregates photogenerated electrons and holes, thereby optimizing the photocatalytic oxidation of triazophos. This study introduces a novel nanocomposite material, characterized by oxygen defects and the S-scheme heterojunction, capable of effectively degrading triazophos and promoting environmental health.

Keywords: photocatalytic; nanocomposites; heterojunction; S-scheme; oxygen defects

Citation: Li, W.; Chen, C.; Yang, R.; Cheng, S.; Sang, X.; Zhang, M.; Zhang, J.; Wang, Z.; Li, Z. Efficient and Stable Degradation of Triazophos Pesticide by TiO_2/WO_3 Nanocomposites with S-Scheme Heterojunctions and Oxygen Defects. *Catalysts* **2023**, *13*, 1136. https://doi.org/10.3390/catal13071136

Academic Editor: Petr Praus

Received: 21 June 2023
Revised: 14 July 2023
Accepted: 19 July 2023
Published: 21 July 2023

1. Introduction

The escalating deployment of organophosphorus pesticides in global agricultural practices has precipitated a severe ecological crisis [1–4]. These anthropogenic compounds, considered integral to modern agricultural methodologies, permeate diverse ecosystems, disrupting the intricate balance of biodiversity and threatening the vitality and sustainability of our planet [5–8]. This precarious situation underscores the urgent need for safe and effective strategies to mitigate the harmful effects of organophosphorus pesticides, particularly triazophos [9–11]. In this regard, photocatalytic technology emerges as a promising solution [12–15]. Over recent years, the photocatalytic degradation of organic pollutants has evolved into an efficient, sustainable, and environmentally friendly strategy for detoxifying polluted aquatic and terrestrial environments [16–19]. This technology, which employs a

specific catalyst to generate potent oxidizing free radicals through photocatalysis, can effectively degrade a broad spectrum of pollutants, including organophosphorus pesticides. Its appeal extends beyond efficiency, encompassing scalability and the potential for seamless integration into existing environmental remediation strategies [20–22].

Oxidative materials with oxygen vacancies have attracted substantial academic attention over the years. These vacancies can act as electron traps, capturing photo-generated electrons and reducing electron–hole recombination, thereby enhancing the efficiency of photocatalytic reactions [23–25]. Moreover, these vacancies can increase the number of active sites on the material surface, strengthening its interaction with reactant molecules and boosting catalytic activity. In the context of photocatalysis, these trapped electrons and the corresponding holes can react with water or oxygen to generate oxidative radicals such as hydroxyl radicals and superoxide anions. These radicals, with their potent oxidative abilities, can degrade organic pollutants, playing a crucial role in environmental remediation and pollution control. However, the inherent limitations of single materials (such as TiO_2, WO_3, CeO_2, etc.), including band gap deficiencies, stability issues, and inefficiencies in photogenerated electron and hole separation, hinder their further development. To overcome these challenges, composite materials, which can compensate for the band gap deficiencies of individual materials and efficiently segregate photogenerated electrons and holes [26–30], are gaining increasing attention, thereby enhancing the generation of oxidative radicals and the overall photocatalytic performance.

A growing body of research indicates that composite material photocatalysts outperform their single-component counterparts in terms of photocatalytic activity. For instance, Liu et al. synthesized ZnO/g-C_3N_4 nanocomposites that exhibited superior activity in H_2O_2 production [31], while Wang et al. $TiO_2/ZnIn_2S_4$ photocatalyst demonstrated commendable activity in CO_2 reduction [32]. Similarly, the TiO_2/Fe_2O_3 composite engineered by Mirmasoomi et al. exhibited remarkable activity in photocatalytic pesticide degradation [33]. Zhang et al. performed a one-pot synthesis of S-scheme WO_3/BiOBr heterojunction nanoflowers, enriched with oxygen vacancies, and exhibited enhanced photodegradation of tetracycline [34]. It is noteworthy that TiO_2, while a common photocatalyst, does not absorb in the visible range. However, WO_3 with oxygen defects exhibits significant visible light absorption characteristics, making it a promising material for the creation of heterostructures such as the TiO_2/WO_3 (TO/WO) nanocomposites in our study.

Motivated by these findings, we attempted the development and characterization of TO/WO nanocomposites, marking a pioneering stride towards triazophos degradation. In our study, TO/WO exhibited exceptional photocatalytic hydrogen evolution activity and stability. Notably, 60-TO/WO demonstrated superior photocatalytic degradation performance, achieving a triazophos degradation rate of 78% within 120 min and retaining commendable photocatalytic stability over four cycles, significantly outperforming TO and WO. This study also confirmed the existence of a substantial number of oxygen vacancies in WO via electron paramagnetic resonance (EPR). The operational mechanism at the TO/WO nanocomposite heterojunction was confirmed as an S-scheme through EPR and theoretical calculations. The presence of oxygen vacancies can expedite charge transfer and enhance the photocatalytic reaction. Similarly, the existence of the S-scheme can effectively segregate photogenerated electron and hole pairs, thereby improving the efficiency of the photocatalytic reaction. This project introduces a TO/WO nanocomposite material characterized by oxygen vacancies and an S-scheme heterojunction, offering a viable approach for pesticide residue elimination.

2. Results

2.1. Phase and Microscopic Morphology Analysis

XRD can be utilized to obtain clear insights into the synthesized materials, as shown in Figure 1a. The results revealed that the XRD peak positions of TO corresponded completely to the tetragonal TiO_2 (no. 78-2486) without any impurities. The XRD peak shapes of WO corresponded completely to the monoclinic WO_3 (no. 83-0950) without any im-

purities. These findings indicate the successful preparation of WO and TO without the presence of amorphous substances. Additionally, in the TO/WO nanocomposites, as the WO ratio gradually increased, the peaks of TO (101) and WO (200) faces became more pronounced. This suggests the presence of both WO and TO crystalline phases in the TO/WO nanocomposites.

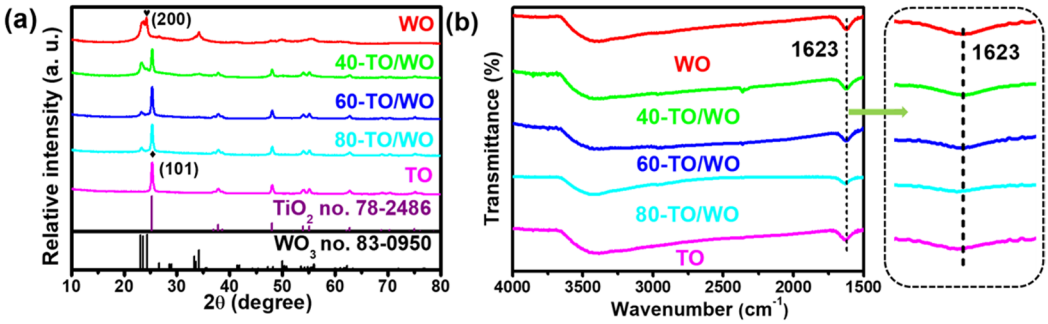

Figure 1. (**a**) The XRD spectra of the samples. (**b**) FT-IR spectra of the samples.

Figure 1b displays the FT-IR spectra of the measured samples. The results indicate that, as the TO proportion increased, the vibrational band at 1623 cm^{-1} of the tested samples gradually shifted to a lower wavenumber, a change that is more clearly observed in the right panel of Figure 1b, implying changes in the chemical bonds within the material after composite formation. Combined with Figure 1a, this indirectly indicates the formation of the composite material in the TO/WO nanocomposites.

SEM and TEM can be employed to analyze the micro-morphology of the synthesized materials. Figure 2a–c show the SEM images of WO, TO, and 60-TO/WO nanocomposites. The results reveal that WO displayed a morphology of multilayered nano-sheets, with a thickness less than 10 nm, while TO existed in the form of nanoparticles with a diameter of approximately 20 nm. In the 60-TO/WO nanocomposite, TO nanoparticles randomly adhered to the WO surface. TEM images (Figure 2d–f) offer more detailed information, demonstrating the aforementioned results. After ultrasonic dispersion, WO presented a ribbon-like shape of nanosheets, and TO was observed as nanoparticles, whereas the 60-TO/WO nanocomposites exhibited a wrapping form between TO nanoparticles and WO nanosheets. The inset in Figure 2f shows the high-resolution TEM image of the 60-TO/WO nanocomposite, where the lattice fringes of TO and WO are observed with d-spacings of 0.350 nm (corresponding to the (101) plane of TO) and 0.361 nm (corresponding to the (200) plane of WO). Furthermore, the presence of heterojunctions, as indicated by the distorted lattice lines represented by the blue line, attests to the successful preparation of the composite material.

Figure 2g displays the SEM energy-dispersive X-ray spectroscopy (EDS) image of the 60-TO/WO nanocomposite, indicating that the sample only contains four elements (C, O, W, and Ti), with no impurity peaks, where C originated from the conductive adhesive, W and O came from WO, and Ti came from TO. This suggests that the 60-TO/WO nanocomposites only contain the constituent elements, demonstrating the sample purity. Figure 2h presents the TEM high-angle annular dark-field (HAADF) and mapping images of the 60-TO/WO nanocomposites, indicating that the distribution of W, O, and Ti elements in the nanocomposites is uniform, confirming the sample's uniformity.

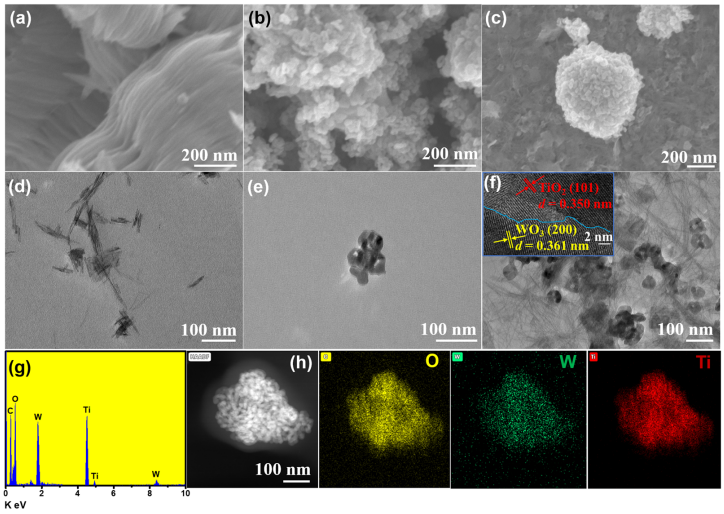

Figure 2. SEM image of (**a**) WO, (**b**) TO, and (**c**) 60-TO/WO nanocomposites. TEM image of (**d**) WO, (**e**) TO, and (**f**) 60-TO/WO nanocomposites (the inset in Figure 2f is the HRTEM image of 60-TO/WO nanocomposite). EDS spectrum of (**g**) 60-TO/WO nanocomposites. HAADF and elemental mapping images of (**h**) 60-TO/WO nanocomposites.

2.2. XPS and Elemental Analysis

XPS can effectively analyze the photoelectron spectra, elemental composition, and chemical structure of the tested materials. Figure 3a shows the XPS full-spectrum image of the 60-TO/WO nanocomposites containing all elements of WO and TO. Furthermore, as depicted in Figure 3a, an array of prominent peaks is discernible in the patterns for TO, WO, and the 60-TO/WO combination. We concentrated our analytical efforts on several ubiquitous peaks. High-resolution XPS element spectra of TO, WO, and 60-TO/WO nanocomposites are displayed in Figure 3b–d. Figure 3b shows that the W 4f of WO exhibits four characteristic peaks, with two more significant peaks of W $4f_{5/2}$ and W $4f_{7/2}$. After computer fitting, two other apparent peaks, both representing W^{5+} ions, are observed, indicating oxygen defects in WO. Additionally, the W 4f peaks of 60-TO/WO nanocomposites demonstrated a shift to the right compared to WO. In Figure 3c, O 1s exhibited two prominent peaks of lattice oxygen and adsorbed oxygen. Furthermore, the 60-TO/WO nanocomposites showed an apparent right shift relative to WO and a clear left shift relative to TO. In Figure 3d, Ti 2p exhibited two obvious peaks of Ti $2p_{1/2}$ and Ti $2p_{3/2}$. Relative to TO, the 60-TO/WO nanocomposite's two peak positions of the Ti 2p exhibited a considerable left shift.

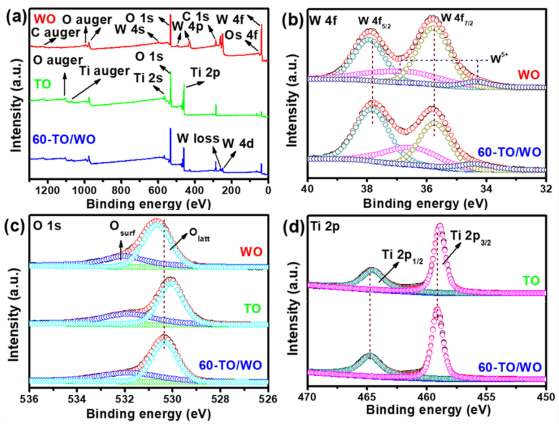

Figure 3. Comparison of (**a**) survey scan, (**b**) W 4f; (**c**) O 1s, (**d**) Ti 2p XPS curves of WO, TO, and 60-TO/WO nanocomposites.

Overall, the 60-TO/WO nanocomposites exhibited a right shift relative to WO and a left shift relative to TO. This demonstrates that the chemical environment on the material surface changed after combining. Different materials may undergo interface reactions, leading to the formation of new chemical environments, indicating the successful fabrication of composite materials. Furthermore, the shifting phenomenon reveals that electron transfer occurred from TO to WO after the composite formation, indicating the formation of a built-in electric field, which is a necessary process for the formation of the S-scheme heterojunction [35–37].

2.3. Specific Surface Area

The BET (Brunauer–Emmett–Teller) technique can effectively be used to observe the pore size distribution of the test sample, specific surface area, and the adsorption isotherm type of N_2. As shown in Figure 4a, all samples exhibited classic Type IV and H3 hysteresis loops, which are commonly found in mesoporous materials with pore sizes within 2–50 nm [37]. The pore size distribution of all tested samples mainly concentrated within 2–50 nm, indicating that they are mesoporous materials.

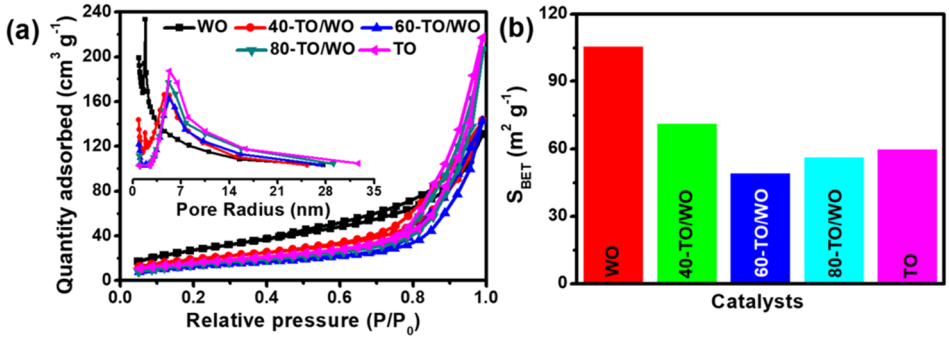

Figure 4. (**a**) N_2 adsorption-desorption isotherms and pore size distribution curves (insert) of TO, WO, and TO/WO nanocomposites; (**b**) The S_{BET} for the TO, WO, and TO/WO nanocomposites.

Figure 4b shows that with the addition of WO, the specific surface area (S_{BET}) of the composite material gradually decreased, with the lowest S_{BET} observed at a WO ratio of 40% (60-TO/WO). This is because increasing the proportion of a single component in the composite material will increase the size and number of catalyst crystal particles based on that component, resulting in a decrease in specific surface area. When the number of new crystal particles in the catalyst increases, even larger aggregates are formed, resulting in a further decrease in S_{BET}. However, when a certain proportion is reached, the effect of the new component on the S_{BET} of the composite material reaches a minimum, and further reducing the proportion of this component will lead to a decrease in the number of crystal particles, resulting in an increase in S_{BET}. In photocatalytic reactions, when the proportion of a particular component increases, the new component may improve the crystal structure or composition inside the photocatalyst, leading to a more excellent crystal structure and catalytic activity. Despite the fact that the new crystal structure usually leads to a decrease in S_{BET}, adjusting the component ratio appropriately can effectively improve the efficiency of photocatalytic reactions, promote the progression of reactions, and accelerate the reaction rate.

2.4. Optical Property and Band Gap Analysis

The UV-vis DRS technique can effectively provide feedback on the light absorption ability and band structure of the photocatalyst. As shown in Figure 5a, WO exhibited visible light excitation characteristics and an obvious tail in WO, TO, and TO/WO nanocomposites. The appearance of the tail often represents the existence of some defects. In the TO/WO nanocomposites, the tail becomes smaller as the proportion of WO gradually increases.

When the content of WO is 0, that is, only TO is present, there is no tail, which indicates the absence of defects.

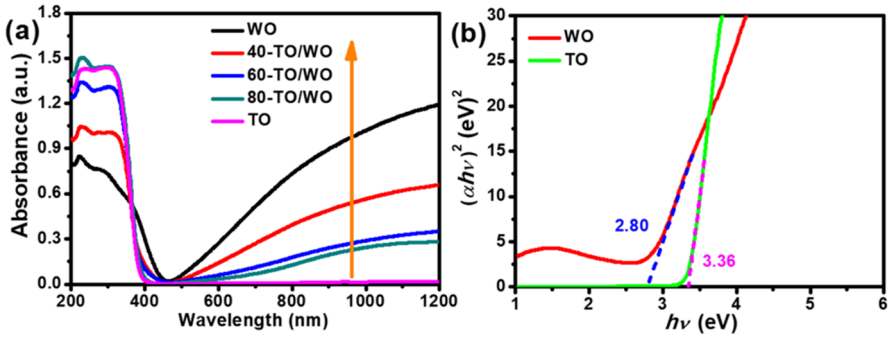

Figure 5. (**a**) UV-vis DRS of WO, TO, and TO/WO nanocomposites. (**b**) Tauc plots of $(\alpha h\nu)^2$ versus energy ($h\nu$) of WO and TO.

Figure 5b, identified as a Tauc plot and obtained by the linear transformation of Figure 5a, presents the band gap diagram of WO and TO. According to Equation (S1) [37] in the Supporting Information, the band gap width of WO and TO was 2.80 and 3.36 eV, respectively. Additionally, based on Formulas (S2) and (S3) [37] in the Supporting Information, the conduction bands of WO and TO were 0.69 and −0.37 eV, respectively, and the valence bands were 3.49 and 2.99 eV, respectively.

2.5. Photocatalytic Performance of Triazophos and Electrochemical Analysis

The photocatalytic activity can intuitively reflect the degradation ability of WO, TO, and TO/WO nanocomposites towards triazophos. As shown in Figure 6a, under simulated sunlight irradiation, both TO and WO exhibited moderate photocatalytic degradation activity. However, when WO and TO form nanocomposites, the TO/WO nanocomposites showed excellent photocatalytic degradation activity. Among them, the 60-TO/WO nanocomposite material had the highest degradation efficiency of triazophos, with a degradation rate of 78% within 120 min. This can be more intuitively represented in Figure 6b. Figure 6c shows the linear relationship between $\ln C_0/C$ and time. The results indicate that the 60-TO/WO nanocomposite material had the highest K_{app} value of 0.021 min^{-1}, which was 2.01 and 2.84 times that of WO and TO, respectively. In comparison to other studies (Table S2), our photodegradation performance exhibited superior results. Figure 6d shows the photocatalytic degradation stability test of TO, WO, and the 60-TO/WO nanocomposites. The results show that the 60-TO/WO nanocomposite material had the optimal photocatalytic degradation stability and can maintain high activity degradation within four cycles.

Photocurrent and impedance are key parameters for evaluating the activity and performance of photocatalysts. Photocurrents can evaluate the photocatalytic activity and electron transfer ability of the catalyst, while impedance can be used to study the charge transfer rate and mechanism in photocatalytic reactions. By analyzing the electrochemical impedance and photocurrent of the photocatalyst, the performance of the catalyst can be optimized and the reaction mechanism of photocatalytic reactions can be further understood. As shown in Figure 7a, TO and WO had obvious photocurrent response curves, while the 60-TO/WO nanocomposite material had the strongest photocurrent response curve. This indicates that the 60-TO/WO nanocomposite material had the best photoreaction characteristics, which is consistent with the results in Figure 6. In Figure 7b, the 60-TO/WO nanocomposite material had the smallest radius, indicating that it had the lowest impedance value, indirectly indicating that the amount of charge passing through the 60-TO/WO nanocomposite material per unit time was the largest, which is beneficial to the progress of photocatalytic reactions.

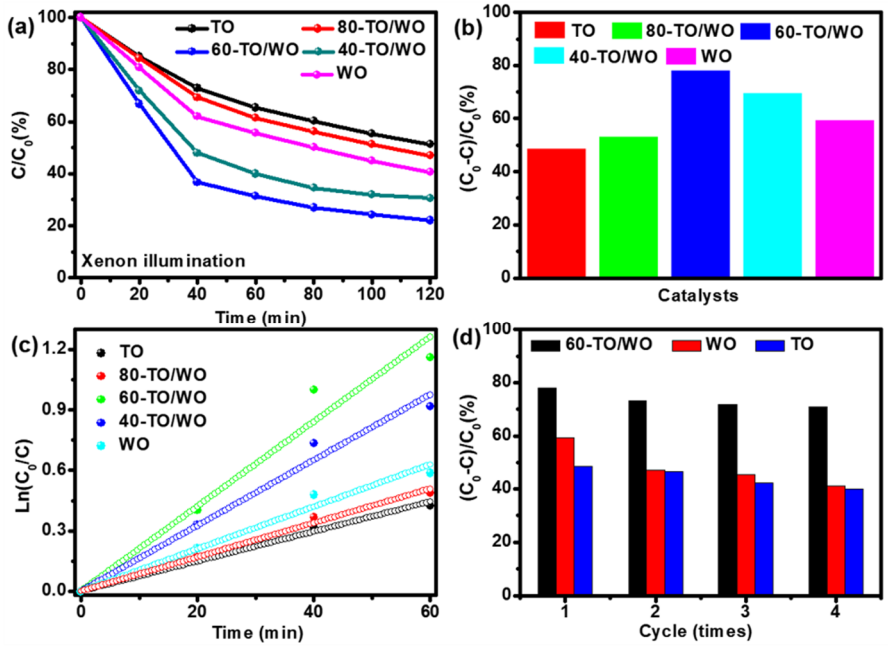

Figure 6. (**a**) The photocatalytic degradation of triazophos. (**b**) The histogram of photocatalytic degradation of triazophos. (**c**) The linear transform ln(C_0/C) vs. times curves of triazophos degradation. (**d**) The photodegradation performance of photocatalysts over four cycles.

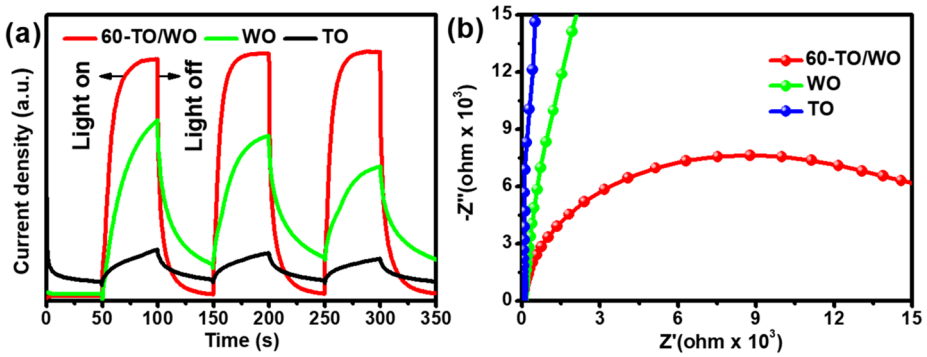

Figure 7. (**a**) Photocurrent density–time curves of TO, WO, and 60-TO/WO nanocomposites. (**b**) Nyquist plots of TO, WO, and 60-TO/WO nanocomposites.

2.6. The Exploration Process of Photocatalytic Mechanism

According to the above results, the energy band structure of WO and TO is staggered, and, thus, the mechanism type of the heterojunction in the TO/WO nanocomposite material may be either Type-II or S-scheme (as shown in Figure 8a). Assuming the mechanism type of the heterojunction in the TO/WO nanocomposite material as Type-II, its effective conduction and valence bands were 0.69 and 3.49 eV, respectively. The conduction band position was evidently lower than the $O_2/\cdot O_2^{-1}$ (−0.33 eV) potential, theoretically incapable of generating $\cdot O_2^{-1}$ effectively. Nonetheless, in testing the 60-TO/WO nanocomposite material, clear $\cdot O_2^{-1}$ signals were observed (as in Figure 8b). This indicates that the mechanism type of the heterojunction in the TO/WO nanocomposite material as Type-II is erroneous. Assuming the mechanism type of the heterojunction in the TO/WO nanocomposite material as S-scheme, its effective conduction band was −0.37 eV, higher than the $O_2/\cdot O_2^{-1}$ potential, theoretically capable of generating $\cdot O_2^{-1}$. This result conforms with the experimental findings, allowing us to infer that the mechanism type of the heterojunction in the TO/WO nanocomposite material is S-scheme. In addition to $\cdot O_2^{-1}$, the presence of hydroxyl radicals (·OH), known to be stronger oxidants, was also detected (as shown

in Figure 8b). The detection of ·OH further demonstrates the photocatalytic activity of the TO/WO nanocomposite material. Furthermore, when testing for the $\cdot O_2^{-1}$ signal in the 60-TO/WO nanocomposite material, we also tested for WO's oxygen defects (as in Figure 8c). The results showed that WO has noticeable oxygen defects. Oxygen defects can increase the surface defect density of a photocatalyst, thereby increasing the chance of adsorbing reactant molecules and accelerating catalytic reactions. Simultaneously, oxygen defects can change the energy band structure of a photocatalyst, expand the photocatalytic spectral range, and improve the photocatalytic activity of the catalyst. Moreover, oxygen defects can also improve the stability of a photocatalyst, reduce the loss of reactants, and prolong the catalyst's life span [38–42]. This is an important factor for the exceptional photocatalytic degradation activity and stability of the 60-TO/WO nanocomposite material.

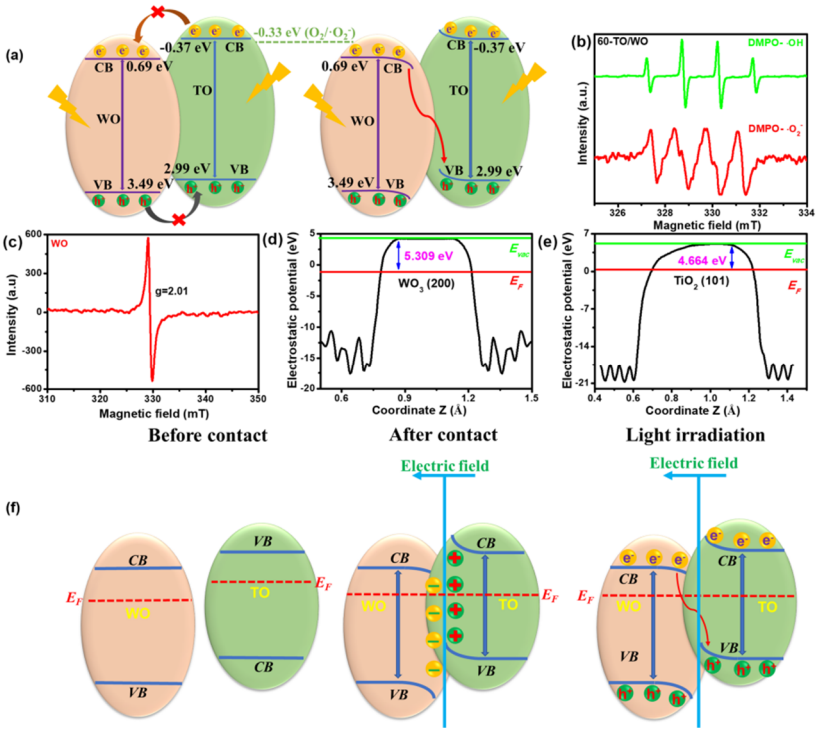

Figure 8. (**a**) The schematic diagrams of charge transfer in Type-II and S-scheme heterojunction. (**b**) DMPO spin trapping EPR spectra of 60-TO/WO nanocomposites ($\cdot O_2^-$ and ·OH). (**c**) Capture the EPR spectra of WO atomic defects. The work function of (**d**) WO (200) and (**e**) TO (101) facet. (**f**) Diagram of the formation process of the S-scheme at the TO/WO nanocomposites heterojunction.

To further determine the mechanism of the heterojunction in the TO/WO nanocomposite material, we calculated the surface work functions of the WO (200) and the TO (101) surfaces through theoretical calculations (as in Figure 8d,e). The results show that the surface work function values of the WO (200) and the TO (101) surfaces were 5.309 and 4.664 eV, respectively. This indicates that the Fermi energy level (E_f) of the WO (200) surface was more negative than that of the TO (101) surface. When WO couples with TO, electrons migrated from TO to WO, thereby achieving the equilibrium state of E_f and forming an internal electric field, as shown in Figure 8f. Consequently, the mechanism type of the heterojunction in the TO/WO nanocomposite material is S-scheme.

2.7. Photocatalytic Mechanism

In summary, we constructed a schematic diagram for the photocatalytic hydrogen production mechanism of TO/WO nanocomposites with S-scheme heterojunction. As shown in Figure 9, under the action of sunlight without any catalysts, the photogenerated electron-hole pairs in TO and WO will be separated and aggregated on their respective

conduction and valence band surfaces. Due to the presence of S-scheme heterojunction, the electron on the WO conduction band surface and the hole on the TO valence band surface will combine and consume each other. At the same time, there will be a large number of photogenerated holes and electrons on the WO valence band surface and the TO conduction band surface, respectively. The multitude of photogenerated electrons on the TO conduction band surface will react with O_2 to generate $\cdot O_2{}^{-1}$. Meanwhile, the photogenerated holes on the WO valence band surface will react with H_2O/OH^- to generate ·OH. $\cdot O_2{}^{-1}$ and ·OH will react with triazophos to oxidize it into CO_2, H_2O, and other non-toxic or low-toxic substances. The presence of S-scheme heterojunction and oxygen vacancies ensures the effective separation of photogenerated electrons and holes in the TO/WO nanocomposites, accelerates the catalytic reaction, improves the stability of the photocatalyst, and enables efficient and continuous photodegradation of triazophos by 60-TO/WO nanocomposites.

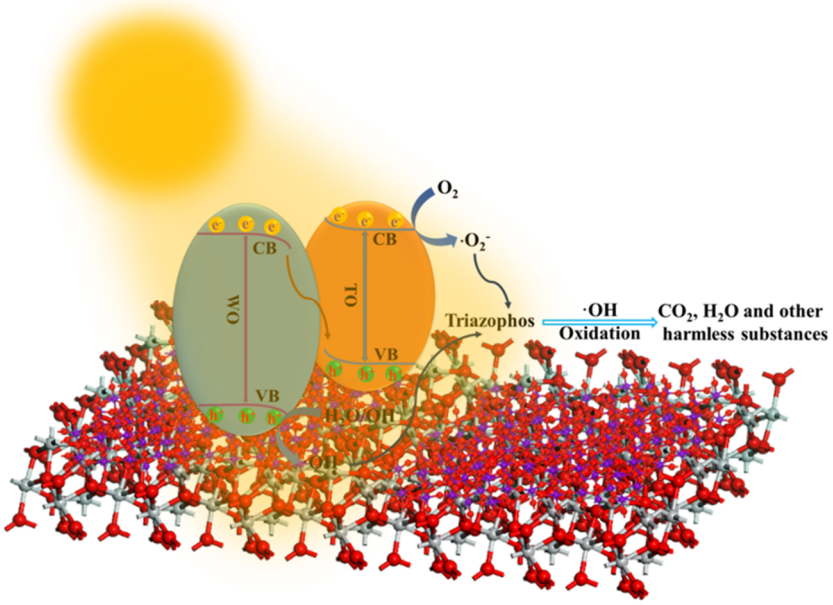

Figure 9. The photocatalysis mechanism of TO/WO nanocomposites under sunlight irradiation without co-catalysts.

3. Experimental

3.1. Material

Tungsten hexachloride (WCl_6), 1-propanol (C_3H_8O), TiO_2, acetylthiocholine iodide, 5,5′-dithiobis (2-nitrobenzoic acid), cholinesterase, nafion, anhydrous ethanol, triazophos, and distilled water were used in this work.

3.2. Synthesis of WO Nanosheets

WO nanosheets were synthesized using a hydrothermal method. This involved the preparation of a solution comprising 35 mL of C_3H_8O and 0.5 g of WCl_6. The solution was transferred to a reaction kettle and underwent a heat treatment at a temperature of 180 °C for a duration of 3 h. This resulted in the formation of WO nanosheets.

3.3. Synthesis of TO/WO Nanocomposites

The synthesis of TO/WO nanocomposites followed a similar process (as shown in Scheme 1). A mixture of 200 mg of TO, 232.52 mg of WCl_6, and 35 mL of C_3H_8O was prepared and stirred thoroughly for an hour. This mixture was then transferred to a 50 mL capacity hydrothermal autoclave and subjected to a heat treatment at 180 °C for 3 h. Following the heat treatment, the product underwent a series of four washing cycles and

was subsequently freeze-dried at temperatures below −45 °C for over 18 h, resulting in the 60-TO/WO nanocomposites.

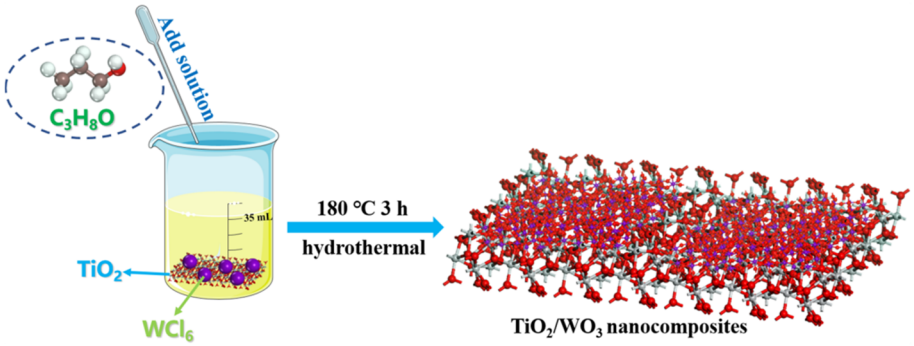

Scheme 1. Synthetic flowchart of TO/WO nanocomposites.

The process for other TO/WO nanocomposites followed the same steps with alterations in the quantities of the raw materials, as detailed in Table S1. The notable difference in the synthesis process of WO and TO/WO nanocomposites was the inclusion or omission of TO in the initial solution.

3.4. Characterization

The current study employed a range of advanced analytical techniques to analyze the samples. X-ray diffraction (XRD) analysis was conducted with the Bruker D8 Advance diffractometer (Bruker Corporation, Billerica, MA, USA), while X-ray photoelectron spectroscopy (XPS) was used to determine surface composition with the ESCALab MKII spectrometer (Thermo Fisher Scientific, Waltham, MA, USA), utilizing powder samples pressed into tablets. Scanning electron microscopy (SEM) and transmission electron microscopy (TEM) were carried out using the Hitachi S-8100 (Hitachi High-Technologies, Tokyo, Japan) and FEI Tecnai G^2-20 microscopes (Thermo Fisher Scientific, Waltham, MA, USA), respectively. Fourier-transform infrared spectroscopy (FT-IR) and ultraviolet-visible diffuse reflectance spectroscopy (UV-vis DRS) were performed using the IR-21 (Shimadzu Corporation, Kyoto, Japan) and Shimadzu UV-2450 spectrometers (Shimadzu Corporation, Kyoto, Japan), respectively. The Micromeritics ASAP 2460 analyzer (Micromeritics Instrument Corp., Norcross, GA, USA) was employed to determine the nitrogen adsorption–desorption isotherms. The inhibition rate of triazophos was evaluated using the pesticide residue detector (Model CXWL-NY-2280-6, Upsilon Instruments Co., Ltd., Huizhou, China). To measure the photoelectrochemical properties, a three-electrode cell was employed, controlled by the CHI-760E electrochemical analyzer (Chenhua Instrument Company, Shanghai, China), with 0.5 M Na_2SO_4 serving as the electrolyte solution. The working electrode was prepared by mixing 10 mg of the catalyst with 10 µL of 5% Nafion and 0.1 mL of ethyl alcohol to form a slurry, which was then coated onto an ITO glass (1.0 cm^2).

3.5. Evaluation of Photocatalytic Activity

The evaluation of the photocatalytic activity was facilitated through a systematic procedure. The experiment commenced with the preparation of a test solution incorporating triazophos pesticide and a buffer solution. A control experiment was simultaneously conducted using only the buffer solution.

Enzymes and a chromogenic agent were added to each of the solutions which then underwent an incubation period. The conditions for incubation were carefully controlled, with a consistent temperature of 37 °C being maintained; room temperature incubation was allowed if the ambient environment was above 20 °C.

Subsequent to this, a substrate was added to each test tube. The process then involved a calibration phase with the light source, as well as the placement of the colorimetric dish into the instrument's colorimetric channel. Illumination during the experiment was

provided by a 300 W xenon lamp (Beijing Zhongjiao Jinyuan Technology Co., Ltd., Beijing, China). A specific detail to note was the maintenance of a 10 cm distance between the lamp and the test solution. Evaluative testing was carried out at 40 min intervals until a steady degradation rate value was observed.

During the entirety of the experiment, precautions were implemented to prevent cross-contamination. This included changing the pipette tip each time the chromogenic agent, substrate, and enzyme were introduced. The conclusion of the experiment was marked by pressing the 'test' button on the instrument, with results being available after a waiting period of 3 min.

4. Conclusions

In conclusion, this study investigated the efficacy of TO/WO nanocomposites, distinguished by oxygen vacancies and S-scheme heterojunctions, as a proficient and eco-friendly methodology for the degradation of triazophosphine pesticides, exhibiting superior photocatalytic activity and robust stability. Within the investigative ensemble, the 60-TO/WO nanocomposites demonstrated exceptional photocatalytic prowess, achieving a degradation rate of 78% within a span of 120 min and maintaining this high caliber of performance across four cycles. Importantly, this research validated the presence of oxygen deficits using EPR. The existence of S-scheme heterojunctions within the nanocomposites was substantiated through EPR and theoretical computations. The presence of oxygen vacancies can expedite charge transfer and effectively augment the photocatalytic reaction. Similarly, the S-scheme can efficiently segregate photogenerated electron and hole pairs, thereby enhancing the efficiency of the photocatalytic reaction. Consequently, TO/WO nanocomposites are poised as promising candidates for future research and development, fostering anticipation for their broader application in environmentally sustainable remediation strategies.

Supplementary Materials: The following supporting information can be downloaded at: https://www.mdpi.com/article/10.3390/catal13071136/s1, Table S1: The amounts of chemicals for preparing WO and TO/WO nanocomposites, Table S2: This work is compared with the work in the literature. References [43–49] are cited in the Supplementary Materials.

Author Contributions: Conceptualization, W.L., C.C. and S.C.; methodology, R.Y.; software, X.S.; validation, W.L., M.Z. and Z.L.; formal analysis, Z.L.; investigation, Z.L.; resources, Z.W. and J.Z.; data curation, Z.L.; writing—original draft preparation, Z.L. and W.L.; writing—review and editing, Z.L. and W.L.; visualization, Z.L. and W.L.; supervision, Z.L. and W.L.; project administration, Z.W. and J.Z.; funding acquisition, Z.L., Z.W. and J.Z. All authors have read and agreed to the published version of the manuscript.

Funding: This work was supported by the National Natural Science Foundation of China (no. 51973078), the Natural Science Foundation of Anhui Province (2108085MB48), the Major Foundation of Educational Commission of Anhui Province (2022AH040068), the Anhui Science and Technology University Introduction of Talents Project SPYJ202201 (200331).

Data Availability Statement: The data presented in this study can be obtained from the first author.

Conflicts of Interest: The authors declare no conflict of interest.

References

1. Bose, S.; Kumar, P.S.; Vo, D.-V.N. A review on the microbial degradation of chlorpyrifos and its metabolite TCP. *Chemosphere* **2021**, *283*, 131447. [CrossRef] [PubMed]
2. Dash, D.M.; Osborne, W.J. A systematic review on the implementation of advanced and evolutionary biotechnological tools for efficient bioremediation of organophosphorus pesticides. *Chemosphere* **2023**, *313*, 137506. [CrossRef] [PubMed]
3. Fu, H.; Tan, P.; Wang, R.; Li, S.; Liu, H.; Yang, Y.; Wu, Z. Advances in organophosphorus pesticides pollution: Current status and challenges in ecotoxicological, sustainable agriculture, and degradation strategies. *J. Hazard. Mater.* **2022**, *424*, 127494. [CrossRef]
4. Gong, C.; Fan, Y.; Zhao, H. Recent advances and perspectives of enzyme-based optical biosensing for organophosphorus pesticides detection. *Talanta* **2022**, *240*, 123145. [CrossRef] [PubMed]
5. Issaka, E.; Wariboko, M.A.; Johnson, N.A.N.; Nyame-do Aniagyei, O. Advanced visual sensing techniques for on-site detection of pesticide residue in water environments. *Heliyon* **2023**, *9*, e13986. [CrossRef]

6. Jain, U.; Saxena, K.; Hooda, V.; Balayan, S.; Singh, A.P.; Tikadar, M.; Chauhan, N. Emerging vistas on pesticides detection based on electrochemical biosensors—An update. *Food Chem.* **2022**, *371*, 131126. [CrossRef]
7. Kou, J.; Li, X.; Zhang, M.; Wang, L.; Hu, L.; Liu, X.; Mei, S.; Xu, G. Accumulative levels, temporal and spatial distribution of common chemical pollutants in the blood of Chinese adults. *Environ. Pollut.* **2022**, *311*, 119980. [CrossRef]
8. Li, H.; Jiao, Y.; Li, L.; Jiao, X. Research progress and trend of effects of organophosphorus pesticides on aquatic organisms in the past decade. *Comp. Biochem. Physiol. C* **2023**, *271*, 109673. [CrossRef]
9. Mali, H.; Shah, C.; Patel, D.H.; Trivedi, U.; Subramanian, R.B. Bio-catalytic system of metallohydrolases for remediation of neurotoxin organophosphates and applications with a future vision. *J. Inorg. Biochem.* **2022**, *231*, 111771. [CrossRef] [PubMed]
10. Matula, M.; Kucera, T.; Soukup, O.; Pejchal, J. Enzymatic Degradation of Organophosphorus Pesticides and Nerve Agents by EC: 3.1.8.2. *Catalysts* **2020**, *10*, 1365. [CrossRef]
11. Mdeni, N.L.; Adeniji, A.O.; Okoh, A.I.; Okoh, O.O. Analytical Evaluation of Carbamate and Organophosphate Pesticides in Human and Environmental Matrices: A Review. *Molecules* **2022**, *27*, 618. [CrossRef]
12. Nandhini, A.R.; Harshiny, M.; Gummadi, S.N. Chlorpyrifos in environment and food: A critical review of detection methods and degradation pathways. *Environ. Sci. Process. Impacts* **2021**, *23*, 1255–1277. [CrossRef]
13. Paidi, M.K.; Satapute, P.; Haider, M.S.; Udikeri, S.S.; Ramachandra, Y.L.; Vo, D.-V.N.; Govarthanan, M.; Jogaiah, S. Mitigation of organophosphorus insecticides from environment: Residual detoxification by bioweapon catalytic scavengers. *Environ. Res.* **2021**, *200*, 111368. [CrossRef] [PubMed]
14. Raj, A.; Kumar, A. Recent advances in assessment methods and mechanism of microbe-mediated chlorpyrifos remediation. *Environ. Res.* **2022**, *214*, 114011. [CrossRef]
15. Veloo, K.V.; Ibrahim, N.A.S. Analytical Extraction Methods and Sorbents' Development for Simultaneous Determination of Organophosphorus Pesticides' Residues in Food and Water Samples: A Review. *Molecules* **2021**, *26*, 5495. [CrossRef] [PubMed]
16. Verma, M.L.; Rani, V. Biosensors for toxic metals, polychlorinated biphenyls, biological oxygen demand, endocrine disruptors, hormones, dioxin, phenolic and organophosphorus compounds: A review. *Environ. Chem. Lett.* **2021**, *19*, 1657–1666. [CrossRef]
17. Vyas, T.; Singh, V.; Kodgire, P.; Joshi, A. Insights in detection and analysis of organophosphates using organophosphorus acid anhydrolases (OPAA) enzyme-based biosensors. *Crit. Rev. Biotechnol.* **2023**, *43*, 521–539. [CrossRef]
18. Xu, W.; Zhao, S.; Zhang, W.; Wu, H.; Guang, C.; Mu, W. Recent advances and future prospective of organophosphorus-degrading enzymes: Identification, modification, and application. *Crit. Rev. Biotechnol.* **2021**, *41*, 1096–1113. [CrossRef]
19. Zammataro, A.; Santonocito, R.; Pappalardo, A.; Trusso Sfrazzetto, G. Catalytic Degradation of Nerve Agents. *Catalysts* **2020**, *10*, 881. [CrossRef]
20. Zhang, Y.; Zhang, W.; Li, J.; Pang, S.; Mishra, S.; Bhatt, P.; Zeng, D.; Chen, S. Emerging Technologies for Degradation of Dichlorvos: A Review. *Int. J. Env. Res. Public Health* **2021**, *18*, 5789. [CrossRef]
21. Zhang, Y.; Zhou, B.; Chen, H.; Yuan, R. Heterogeneous photocatalytic oxidation for the removal of organophosphorus pollutants from aqueous solutions: A review. *Sci. Total Environ.* **2023**, *856*, 159048. [CrossRef] [PubMed]
22. Zhao, S.; Xu, W.; Zhang, W.; Wu, H.; Guang, C.; Mu, W. Overview of a bioremediation tool: Organophosphorus hydrolase and its significant application in the food, environmental, and therapy fields. *Appl. Microbiol. Biotechnol.* **2021**, *105*, 8241–8253. [CrossRef]
23. Ma, J.; Long, R.; Liu, D.; Low, J.; Xiong, Y. Defect Engineering in Photocatalytic Methane Conversion. *Small Struct.* **2022**, *3*, 2100147. [CrossRef]
24. Sultana, S.; Mansingh, S.; Parida, K.M. Crystal facet and surface defect engineered low dimensional CeO_2 (0D, 1D, 2D) based photocatalytic materials towards energy generation and pollution abatement. *Mater. Adv.* **2021**, *2*, 6942–6983. [CrossRef]
25. Zhao, Y.; Mao, Q.; Zhai, X.; Zhang, G. Structural Defects Regulation of Bismuth Molybdate Photocatalyst. *Prog. Chem.* **2021**, *33*, 1331–1343.
26. Cheng, C.; Zhang, J.; Zhu, B.; Liang, G.; Zhang, L.; Yu, J. Verifying the Charge-Transfer Mechanism in S-Scheme Heterojunctions Using Femtosecond Transient Absorption Spectroscopy. *Angew. Chem.* **2023**, *62*, e202218688. [CrossRef]
27. Xiao, Y.; Tian, X.; Chen, Y.; Xiao, X.; Chen, T.; Wang, Y. Recent Advances in Carbon Nitride-Based S-scheme Photocatalysts for Solar Energy Conversion. *Materials* **2023**, *16*, 3745. [CrossRef]
28. Xu, Q.; Wageh, S.; Al-Ghamdi, A.A.; Li, X. Design principle of S-scheme heterojunction photocatalyst. *J. Mater. Sci. Technol.* **2022**, *124*, 171–173. [CrossRef]
29. Yang, H.; Zhao, Z.-C.; Yang, Y.-P.; Zhang, Z.; Chen, W.; Yan, R.-Q.; Jin, Y.; Zhang, J. Defective WO_3 nanoplates controllably decorated with MIL-101(Fe) nanoparticles to efficiently remove tetracycline hydrochloride by S-scheme mechanism. *Sep. Purif. Technol.* **2022**, *300*, 121846. [CrossRef]
30. Zhang, J.; Zhang, L.; Wang, W.; Yu, J. In Situ Irradiated X-ray Photoelectron Spectroscopy Investigation on Electron Transfer Mechanism in S-Scheme Photocatalyst. *J. Phys. Chem. Lett.* **2022**, *13*, 8462–8469. [CrossRef]
31. Liu, Y.; Jin, Y.; Cheng, X.; Ma, J.; Li, L.; Fan, X.; Ding, Y.; Han, Y.; Tao, R. K+-Doped ZnO/g-C_3N_4 Heterojunction: Controllable Preparation, Efficient Charge Separation, and Excellent Photocatalytic VOC Degradation Performance. *Ind. Eng. Chem. Res.* **2022**, *61*, 187–197. [CrossRef]
32. Wang, K.; Li, X.; Wang, N.; Shen, Q.; Liu, M.; Zhou, J.; Li, N. Z-Scheme Core-Shell meso-TiO_2@$ZnIn_2S_4$/Ti_3C_2 MXene Enhances Visible Light-Driven CO_2-to-CH_4 Selectivity. *Ind. Eng. Chem. Res.* **2021**, *60*, 8720–8732. [CrossRef]
33. Mirmasoomi, S.R.; Ghazi, M.M.; Galedari, M. Photocatalytic degradation of diazinon under visible light using TiO_2/Fe_2O_3 nanocomposite synthesized by ultrasonic-assisted impregnation method. *Sep. Purif. Technol.* **2017**, *175*, 418–427. [CrossRef]

34. Zhang, X.; Huang, W.; Xia, Z.; Xian, M.; Bu, F.; Liang, F.; Feng, D. One-pot synthesis of S-scheme WO_3/BiOBr heterojunction nanoflowers enriched with oxygen vacancies for enhanced tetracycline photodegradation. *Sep. Purif. Technol.* **2022**, *290*, 12087. [CrossRef]
35. Zhang, L.; Zhang, J.; Yu, H.; Yu, J. Emerging S-Scheme Photocatalyst. *Adv. Mater.* **2022**, *34*, 2107668. [CrossRef]
36. Xu, X.T.; Huang, Y.; Dai, K.; Wang, Z.L.; Zhang, J.F. Non-noble-metal CuSe promotes charge separation and photocatalytic CO_2 reduction on porous g-C_3N_4 nanosheets. *Sep. Purif. Technol.* **2023**, *317*, 123887. [CrossRef]
37. Li, Z.; Jin, D.; Wang, Z. $WO_3(H_2O)_{0.333}$/CdSe-diethylenetriamine nanocomposite as a step-scheme photocatalyst for hydrogen production. *Surf. Interfaces* **2022**, *29*, 101702. [CrossRef]
38. Brown, J.J.; Ke, Z.; Ma, T.; Page, A.J. Defect Engineering for Photocatalysis: From Ternary to Perovskite Oxynitrides. *ChemNanoMat* **2020**, *6*, 708–719. [CrossRef]
39. Kumar, A.; Raizada, P.; Khan, A.A.P.; Nguyen, V.-H.; Van Le, Q.; Singh, A.; Saini, V.; Selvasembian, R.; Huynh, T.-T.; Singh, P. Phenolic compounds degradation: Insight into the role and evidence of oxygen vacancy defects engineering on nanomaterials. *Sci. Total Environ.* **2021**, *800*, 149410. [CrossRef]
40. Wang, Q.; Zhang, S.; He, H.; Xie, C.; Tang, Y.; He, C.; Shao, M.; Wang, H. Oxygen Vacancy Engineering in Titanium Dioxide for Sodium Storage. *Chem. Asian J.* **2021**, *16*, 3–19. [CrossRef]
41. Wang, Z.; Lin, R.; Huo, Y.; Li, H.; Wang, L. Formation, Detection, and Function of Oxygen Vacancy in Metal Oxides for Solar Energy Conversion. *Adv. Funct. Mater.* **2022**, *32*, 2109503. [CrossRef]
42. Ye, K.; Li, K.; Lu, Y.; Guo, Z.; Ni, N.; Liu, H.; Huang, Y.; Ji, H.; Wang, P. An overview of advanced methods for the characterization of oxygen vacancies in materials. *TrAC Trends Anal. Chem.* **2019**, *116*, 102–108. [CrossRef]
43. Salarian, A.-A.; Hami, Z.; Mirzaei, N.; Mohseni, S.M.; Asadi, A.; Bahrami, H.; Vosoughi, M.; Alinejad, A.; Zare, M.-R. N-doped TiO_2 nanosheets for photocatalytic degradation and mineralization of diazinon under simulated solar irradiation: Optimization and modeling using a response surface methodology. *J. Mol. Liq.* **2016**, *220*, 183–191. [CrossRef]
44. Pathania, D.; Sharma, A.; Kumar, S.; Srivastava, A.K.; Kumar, A.; Singh, L. Bio-synthesized Cu-ZnO hetro-nanostructure for catalytic degradation of organophosphate chlorpyrifos under solar illumination. *Chemosphere* **2021**, *277*, 130315. [CrossRef] [PubMed]
45. Vigneshwaran, S.; Preethi, J.; Meenakshi, S. Removal of chlorpyrifos, an insecticide using metal free heterogeneous graphitic carbon nitride (g-C_3N_4) incorporated chitosan as catalyst: Photocatalytic and adsorption studies. *Int. J. Biol. Macromol.* **2019**, *132*, 289–299. [CrossRef]
46. Hossaini, H.; Moussavi, G.; Farrokhi, M. Oxidation of diazinon in cns-ZnO/LED photocatalytic process: Catalyst preparation, photocatalytic examination, and toxicity bioassay of oxidation by-products. *Sep. Purif. Technol.* **2017**, *174*, 320–330. [CrossRef]
47. Isari, A.A.; Moradi, S.; Rezaei, S.S.; Ghanbari, F.; Dehghanifard, E.; Kakavandi, B. Peroxymonosulfate catalyzed by core/shell magnetic ZnO photocatalyst towards malathion degradation: Enhancing synergy, catalytic performance and mechanism. *Sep. Purif. Technol.* **2021**, *275*, 119163. [CrossRef]
48. Antonopoulou, M.; Giannakas, A.; Bairamis, F.; Papadaki, M.; Konstantinou, I. Degradation of organophosphorus flame retardant tris (1-chloro-2-propyl) phosphate (TCPP) by visible light N,S-codoped TiO_2 photocatalysts. *Chem. Eng. J.* **2017**, *318*, 231–239. [CrossRef]
49. Tang, Q.-Y.; Chen, W.-F.; Lv, Y.-R.; Yang, S.-Y.; Xu, Y.-H. Z-scheme hierarchical Cu_2S/Bi_2WO_6 composites for improved photocatalytic activity of glyphosate degradation under visible light irradiation. *Sep. Purif. Technol.* **2020**, *236*, 116243. [CrossRef]